



Cite this: *Nanoscale Adv.*, 2023, **5**, 3671

## Biomass-derived carbon deposited $\text{TiO}_2$ nanotube photocatalysts for enhanced hydrogen production

Shaeel Ahmed Althabaiti,<sup>a</sup> Zaheer Khan,<sup>a</sup> Maqsood Ahmad Malik,<sup>ID, \*b</sup> Salem Mohamed Bawaked,<sup>a</sup> Soad Zahir Al-Sheheri,<sup>a</sup> Mohamed Mokhtar,<sup>a</sup> Sharf Ilahi Siddiqui<sup>c</sup> and Katabathini Narasimharao<sup>\*a</sup>

In this study, titanium oxide nanotubes ( $\text{TiO}_2$ NTs) were deposited on the surface of activated carbon (AC) by varying the wt% of AC. The physicochemical properties of synthesized  $\text{TiO}_2$ NTs–AC nanocomposites were analysed by various characterization techniques such as XRD, FT-IR, Raman, DRUV-vis, HR-TEM, XPS, PL, and  $\text{N}_2$  physisorption. The FT-IR, EDX, and XPS analyses proved the existence of interaction between AC and  $\text{TiO}_2$ NTs. This study found that as the content of AC increases, the surface area and pore volume increase while the energy bandgap decreases. The  $\text{TiO}_2$ NTs–AC nanocomposite with 40% AC exhibited a surface area of  $291 \text{ m}^2 \text{ g}^{-1}$ , pore volume of  $0.045 \text{ cm}^3 \text{ g}^{-1}$  and half pore width =  $8.4 \text{ \AA}$  and had a wide band gap energy (3.15 eV). In addition, the photocatalytic application of the prepared nanocomposites for photocatalytic  $\text{H}_2$  production was investigated. The  $\text{H}_2$  was produced *via* photo-reforming in the presence of a sacrificial agent (methanol) under sunlight irradiation. It was found that the prepared  $\text{TiO}_2$ NTs–AC nanocomposite with 40% AC acted as an efficient photocatalyst for aqueous-methanol reforming under various optimization conditions. Approximately  $18\,000 \text{ \mu mol l}^{-1}$  hydrogen gas was produced *via* aqueous-methanol reforming under optimized conditions (catalyst dose = 100 mg, temperature =  $25^\circ\text{C}$ , time = 12 hours, vol. of methanol = 20% (v/v), and pH = 7). The reusability of the  $\text{TiO}_2$ NTs–AC nanocomposite was also investigated for 5 consecutive cycles, and the results suggested only a slight decline in efficiency even after the fifth cycle. This study demonstrates the ability of an activated carbon deposited  $\text{TiO}_2$ NT catalyst to produce hydrogen effectively under sunlight.

Received 2nd April 2023

Accepted 22nd May 2023

DOI: 10.1039/d3na00211j

rsc.li/nanoscale-advances

## 1. Introduction

Along with increasing energy demand, the fossil fuel industry is also growing at an alarming rate. Developed industries release large amounts of emissions, such as greenhouse gases (GHGs) and other air pollutants, into the atmosphere.<sup>1</sup> GHG emissions mainly contain toxic gases such as  $\text{CO}_2$ , NO,  $\text{NO}_2$ , and  $\text{SO}_2$ , which are fatal for humans and the environment.<sup>1,2</sup> Because of this condition, many efforts are being made immediately to reduce fossil fuel production and consumption considerably, although it seems a little far from possible.<sup>3</sup>

At this juncture, hydrogen ( $\text{H}_2$ ) is emerging as an alternative to fossil fuels, which can be used as an excellent carbon-free fuel.<sup>4</sup>  $\text{H}_2$  fuel cells are presently under use for automobiles as  $\text{H}_2$  burning with  $\text{O}_2$  generates only water as a by-product, proving to be a better fuel option.<sup>5,6</sup> Although  $\text{H}_2$  is a clean and green energy source, its production on a large industrial

scale is still un-affordable.<sup>7</sup> The significant aspects which are considered while developing the technology for  $\text{H}_2$  production are: (i) avoiding the generation of GHGs mainly  $\text{CO}_x$ , (ii) long-term supply, and (iii) an economically viable process.<sup>1,2</sup>

Thermal,<sup>8</sup> chemical,<sup>9</sup> biological,<sup>10</sup> electrolytic,<sup>11</sup> photo-electrolytic<sup>12</sup> and photocatalytic processes<sup>13</sup> have been used for  $\text{H}_2$  production. Most of the  $\text{H}_2$  these days is produced through the steam reforming of natural gases, such as methane, following the water gas shift process.<sup>5,6</sup> However, conventional  $\text{H}_2$  production processes require high temperatures and pressure, which does not make these processes sustainable and efficient.<sup>5</sup> Among various processes,  $\text{H}_2$  production *via* water splitting can be recognized as the most prominent method.<sup>14,15</sup> The first reported suitable technology to produce  $\text{H}_2$  *via* water splitting was the photo-assisted electrochemical method. However, it needs sophisticated instrumentations.<sup>15</sup> Recently,  $\text{H}_2$  production occurred on the surface of various semiconductors (photocatalysts) *via* water splitting under light irradiation at ambient temperature, proving to be a better and more sustainable technique.<sup>5,16</sup> The most commonly used photocatalyst is titanium oxide,  $\text{TiO}_2$  (non-toxic, cheap, and chemically stable).<sup>17</sup> However, due to the wide band gap and fast  $e^- - h^+$  recombination, its use could not have been practical for  $\text{H}_2$  production.<sup>5</sup>

<sup>a</sup>Chemistry Department, Faculty of Science, King Abdulaziz University, P.O. Box 80203, Jeddah 21589, Saudi Arabia. E-mail: nkatabathini@kau.edu.sa

<sup>b</sup>Department of Chemistry, Faculty of Natural Sciences, Jamia Millia Islamia, New Delhi, 110025, India. E-mail: mamalik@jmi.ac.in

<sup>c</sup>Department of Chemistry, Ramjas College, University of Delhi, Delhi-07, India



Notably, the criteria to obtain an environmentally friendly and efficient photocatalyst are: (i) efficient absorption of solar light, (ii) stability under working conditions, and (iii) cost-effectiveness to split water into H<sub>2</sub> efficiently.<sup>5–7</sup> These criteria can be achieved by tuning the structure of the photocatalyst to have (a) charge carrier (e<sup>–</sup> and h<sup>+</sup>) separation, (b) delayed e<sup>–</sup> and h<sup>+</sup> recombination and their migration to surface reactive centers, (c) correct alignment of band edges, and (d) avoiding the use of expensive raw materials,<sup>5</sup> although practically this seems less possible as these criteria can only be achieved by doping the photocatalyst with expensive metals such as platinum, palladium, silver, *etc.*<sup>16,18,19</sup> TiO<sub>2</sub> has also been used to produce H<sub>2</sub> by doping different metal species.<sup>16</sup> Other heterogeneous materials have also been made with TiO<sub>2</sub>, although they also did not prove to be very relevant, as their cost was high.<sup>20,21</sup> It should be noted that to make the process more efficient, a sacrificial agent such as methanol, ethanol, lactic acid, *etc.*, has also been used.<sup>5,22</sup> Since the sacrificial agent acts as a source of protons in the water splitting process, the H<sub>2</sub> production rate increases substantially in the presence of the sacrificial agent.<sup>5,23,24</sup> Although semiconductors help produce H<sub>2</sub> through water splitting with sacrificial agents, low-cost and fast production rates under solar light irradiation are still rare.

It is found that the use of AC with semiconductors can be a good step.<sup>25</sup> AC is fairly cheap, providing a good surface that can easily be decorated with semiconductors.<sup>26</sup> It has also been proven from the previous literature that AC combined with semiconductors helps in charge separation (or prevention of e<sup>–</sup> and h<sup>+</sup> recombination) for photocatalysts.<sup>25–27</sup> Therefore, the merging of AC with semiconductors can be a practical option. However, there is hardly any reported study on H<sub>2</sub> production by combining AC with TiO<sub>2</sub>. Therefore, in this study TiO<sub>2</sub>NTs–AC nanocomposites were synthesized and utilized for H<sub>2</sub> production under solar light with sacrificial agent, methanol. This can be a great effort for energy production. This is the first study that has not been reported before. Hence, the objectives of this study could be described as (a) synthesis of AC, (b) synthesis of TiO<sub>2</sub>NTs, (c) synthesis of TiO<sub>2</sub>NTs–AC, (d) characterization of TiO<sub>2</sub>NTs–AC composites, (e) H<sub>2</sub> production investigation, (f) optimization of H<sub>2</sub> production, and (g) reusability of TiO<sub>2</sub>NTs–AC.

## 2. Experimental

### 2.1. Chemicals

Titanium(IV) isopropoxide (TTIP) (Ti[OCH(CH<sub>3</sub>)<sub>2</sub>]<sub>4</sub> – 97%), sodium hydroxide (NaOH – 98%), potassium hydroxide (KOH – 99.95%), and methanol (CH<sub>3</sub>OH – 99.9%) are analytical research grade reagents and were obtained from Sigma Aldrich, UK. The reagents were used as received. In addition, walnut shells were collected from the local market. Deionized water was used for the preparation and activity tests.

### 2.2. Synthesis of materials

#### 2.2.1. Preparation of walnut shell-derived activated carbon (AC).

AC was synthesized using walnut shells, a biomass as

a raw material.<sup>28</sup> In brief, the walnut shells were cleaned and dried under sunlight and then dried in an oven at 100 °C for 10 h. Then, 100 g of walnut shells were crushed well and pulverized. The pulverized shells were taken in a silica crucible and pre-carbonized at 450 °C for 3 h in a muffle furnace. Then, the crucible was allowed to cool to room temperature to obtain a black solid. Next, the product was collected and ground well with a pestle and mortar. To activate the black carbon powder, it was treated with 12% KOH solution for 5 h at 90 °C. Then, the obtained activated carbon slurry was filtered and placed in the open air for 12 h and subsequently transferred into a silica crucible to be thermally treated at 800 °C for 3 h. Next, the AC was washed with dil. HCl (5%) and double-distilled water until the pH of the filtered solution became neutral. Finally, the washed cake was dried at 100 °C for 5 h to remove the moisture and ground into fine AC powder using a pestle and mortar.

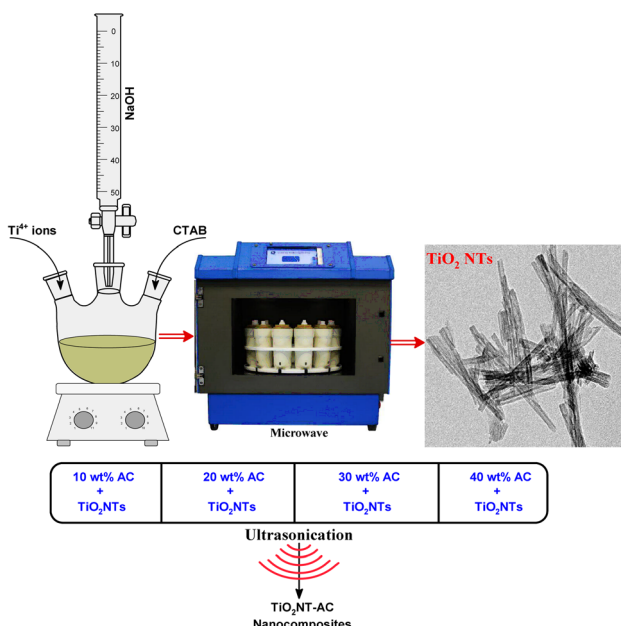
**2.2.2. Synthesis of anatase TiO<sub>2</sub>NTs.** The microwave hydrothermal method was used to produce TiO<sub>2</sub>NTs.<sup>29</sup> At first, 50 mL of boiling water was used to dissolve a predetermined quantity of CTAB. To this, 90 mL of solution containing 2-propanol and TTIP was added while the mixture was being stirred for 1 hour to obtain a homogeneous suspension. To this suspension, 0.2 M NaOH solution was added dropwise to maintain pH 13. Finally, the suspension was transferred into specially designed vessels and the vessels were placed in an ETHOS microwave lab station for microwave hydrothermal treatment. The treatment was continued for 1 h at 120 °C with a microwave power of 500 W under autogenous pressure. After being filtered, the precipitate was washed repeatedly until the pH of the filtrate was near 7. Finally, the washed sample was dried in an oven at 100 °C for 4 h. After this, the substance was calcined in a muffle furnace at 450 °C for 6 h.

**2.2.3. Preparation of TiO<sub>2</sub>NTs–AC nanocomposites.** To make the TiO<sub>2</sub>NTs–AC composites, a predetermined quantity of calcined TiO<sub>2</sub>NTs was dispersed in 25 mL of 2-propanol. A solution of 2-propanol containing 25 mL was stirred continuously while an unknown quantity of AC was mixed in. The treatment was continued for an additional 1 h after the AC dispersion was introduced to the TiO<sub>2</sub>NT solution while it was vigorously stirred and sonicated. After being made into TiO<sub>2</sub>NTs–AC (Scheme 1), it was filtered and then dried in a hot air oven at a temperature of 100 °C for 5 h. Four different composites were prepared by varying the wt% of AC (10, 20, 30, and 40 wt%) over a fixed amount of prepared TiO<sub>2</sub>NT powder.

### 2.3. Characterization

The crystal structures of bare TiO<sub>2</sub>NTs, AC, and TiO<sub>2</sub>NTs–AC were examined using X-ray diffraction (XRD) on a D8 Advance Bruker powder X-ray diffractometer at a 2θ range of 10° to 80°. A Thermo-Fisher Scientific Nicolet iS5 FT-IR spectrometer was used to investigate surface functional groups of the prepared materials. Raman spectra were measured using a micro-Raman spectrometer and an image spectrograph, STR 500 mm Focal Length Laser Raman spectrometer, with a flat field: 27 mm (W) 14 mm (H), and resolution: 1/0.6 cm<sup>–1</sup>/pixel. A Thermo Scientific Evolution 220 diffuse reflectance UV-vis spectrophotometer





**Scheme 1** Synthesis of  $\text{TiO}_2$ NTs and ultrasonic deposition of AC on  $\text{TiO}_2$ NTs.

(DR UV-vis) was used to investigate the optical properties of the as prepared materials in the wavelength range of 220–900 nm. The photoluminescence (PL) spectra were recorded at room temperature on a Varian Cary Eclipse Photoluminescence spectrophotometer. A high-resolution transmission electron microscope (HR-TEM) (FEI-TECNAI G2-20 TWIN with LaB6 filaments) working at 200 kV was used to analyse the morphologies of the produced nanomaterials. An Autosorb-iQ 2ST/MP, Quantachrome, nitrogen gas adsorption–desorption at 77 K was used to determine the specific surface areas of the synthesised materials. Using a Thermo-Scientific Escalab 250 Xi XPS apparatus with Al  $\text{K}\alpha$  X-rays having a spot size of 650 nm, the samples' X-ray photoelectron spectra were obtained.

## 2.4. Photocatalytic utilization of $\text{TiO}_2$ NTs–AC nanocomposites

The photocatalytic reactions were performed using a laboratory build reactor equipped with a 500 W xenon lamp with a light intensity of  $800 \text{ W m}^{-2}$  and photon flux of 650 lm. A double-jacket Pyrex-glass reactor (100 mL volume) was fitted with a quartz window for UV light passage. Before starting the photocatalytic activity tests, the reactor was flushed with argon gas for 20 min. Then, the UV lamp was switched on and waited for 15 minutes to reach stability (light intensity of  $45 \text{ mW cm}^{-2}$ ). The reactor is also equipped with a cold-water circulation system to keep the reaction temperature at  $25^\circ\text{C}$ . To evaluate the photocatalytic efficiency of the synthesized catalysts, 20% of an aqueous methanol solution (0.15 mol methanol) and 100 mg of catalyst were used. At different time intervals, a known product sample (0.5  $\mu\text{L}$ ) was analysed using an Agilent gas chromatograph equipped with a TCD and Carboxen 1000 packed column.<sup>30</sup>

## 3. Results and discussion

### 3.1. XRD analysis

The XRD patterns of the synthesized samples are shown in Fig. 1. The X-ray diffraction patterns of AC and bare  $\text{TiO}_2$ NT samples are compared to that of the  $\text{TiO}_2$ NTs–AC NC (10–40 wt% of AC). The AC sample displayed two characteristic X-ray reflections in the XRD pattern at around  $2\theta$  values of  $25^\circ$  and  $45^\circ$  corresponding to the (002) and (101) planes that feature prominently in the cellulosic carbon framework.<sup>31</sup> Bare  $\text{TiO}_2$ NT samples displayed several characteristic XRD reflections for the anatase  $\text{TiO}_2$  phase at around  $26^\circ$ ,  $38^\circ$ ,  $47^\circ$ ,  $54^\circ$ ,  $56^\circ$ ,  $62^\circ$ ,  $68^\circ$ ,  $69^\circ$ , and  $77^\circ$  accounted for the (101), (004), (200), (105), (211), (204), (116), (220), and (215) planes respectively. The XRD reflections of existing  $\text{TiO}_2$ NTs matched JCPDS file (01-084-1286) of anatase  $\text{TiO}_2$  crystals and showed good agreement with the literature.<sup>32,33</sup> The  $\text{TiO}_2$ NTs–AC (10–40 wt%) composite samples also showed similar XRD peaks as bare  $\text{TiO}_2$ NTs,

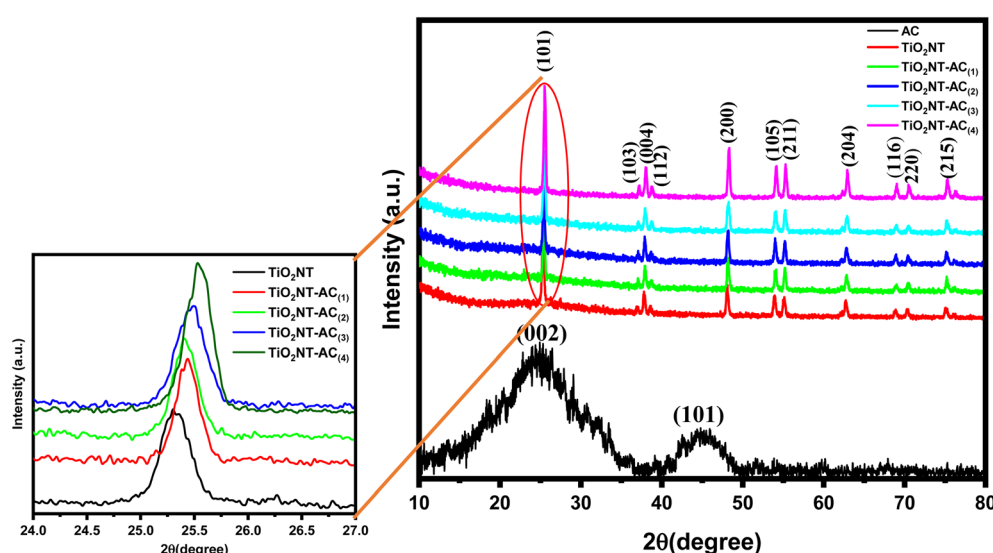


**Fig. 1** XRD patterns of synthesized nanocomposites.

Table 1 The dependence of physicochemical properties of  $\text{TiO}_2\text{NTs-AC}$  at varying AC contents

Sample	$\text{TiO}_2\text{NT}$ crystallite size (nm)	Surface area ( $\text{m}^2 \text{ g}^{-1}$ )	Pore volume ( $\text{cm}^3 \text{ g}^{-1}$ )	Half pore width (Å)	Band gap (eV)
AC	—	634	0.401	8.0	—
Pure $\text{TiO}_2\text{NTs}$	9.27	56	0.014	13.8	3.12
$\text{TiO}_2\text{NT-AC}_{(1)}$	6.31	127	0.020	8.4	3.08
$\text{TiO}_2\text{NT-AC}_{(2)}$	6.32	159	0.023	8.4	3.08
$\text{TiO}_2\text{NT-AC}_{(3)}$	7.49	204	0.036	8.4	3.07
$\text{TiO}_2\text{NT-AC}_{(4)}$	15.07	291	0.045	8.4	3.01

although the intensity of AC-deposited  $\text{TiO}_2\text{NT}$  samples was lower. This could be due to the excellent deposition of  $\text{TiO}_2\text{NTs}$  onto the AC through several possible interactions (electrostatic and non-electrostatic). It has also been noted that no phase change was observed, irrespective of the presence of a large amount of AC. This observation indicates the existence of highly dispersed AC over the surface of the crystalline anatase structure of  $\text{TiO}_2\text{NTs}$ .

The crystallite size was calculated using Scherrer's formula, *i.e.*  $\{D = K\lambda/\beta \cos \theta\}$  where  $K$  is a constant = 0.89,  $\lambda$  is the wavelength of the X-ray radiation,  $\beta$  is the full width at half-maximum, and  $\theta$  is the diffraction angle}, which increases with an increase in AC contents (10 to 40 wt%). The larger crystallite size at higher AC content (40 wt%) resulted because the formation of larger-sized particles might be due to the coalescence of small grains *via* grain boundary diffusion. The change in crystallite size with an increase in AC content is presented in Table 1. Furthermore, XRD profiles did not show any reflections for other impurity phases, which suggests the high phase purity attained by the adapted synthesis method. Similar observations were reported in the previous literature.<sup>34,35</sup>

### 3.2. Raman spectroscopy

Raman spectra of the samples were obtained for a better understanding of the structure and vibrational modes of

crystalline materials. The Raman spectra of  $\text{TiO}_2\text{NTs}$  and  $\text{TiO}_2\text{NTs-AC}$  (10–40 wt%) are shown in Fig. 2. The Raman spectrum of bare  $\text{TiO}_2\text{NTs}$  (see the black line) has shown three peaks at approximately 395.0, 515.0, and 635.0  $\text{cm}^{-1}$  for  $\text{B}_{1g(1)}$ ,  $\text{A}_{1g}$  (+ $\text{B}_{1g(2)}$ ), and  $\text{E}_g$  modes respectively. These peaks were related to the anatase phase of  $\text{TiO}_2$ .<sup>28</sup> The bands belonging to the  $\text{TiO}_2\text{NTs}$  were also observed in all the Raman spectra of  $\text{TiO}_2\text{NT}$ -deposited AC. In addition to  $\text{TiO}_2\text{NT}$  bands, two other bands were found in the Raman spectra of  $\text{TiO}_2\text{NTs-AC}$  samples (in-large inset image). These bands were assigned for the D band ( $\text{sp}^3$ -defective carbon) and G band (ordered  $\text{sp}^2$ -bonded carbon atoms) at approximately 1345.00 and  $\sim$ 1615.00  $\text{cm}^{-1}$ , respectively. A slight shift in the peak position and decrease in peak intensity of the Raman peaks of  $\text{TiO}_2\text{NTs-AC}$  samples confirms the formation of  $\text{TiO}_2\text{NTs-AC}$  composites due to interaction between AC and  $\text{TiO}_2\text{NTs}$ .<sup>34</sup>

### 3.3. FT-IR spectroscopy

To investigate the functional groups present in the synthesized materials (AC, bare  $\text{TiO}_2\text{NTs}$ , and  $\text{TiO}_2\text{NTs-AC}$ ) and the interaction between the functional groups (of AC and  $\text{TiO}_2\text{NTs}$  in  $\text{TiO}_2\text{NTs-AC}$ ), FT-IR spectra of the samples were collected (Fig. 3). The spectrum of the bare  $\text{TiO}_2\text{NT}$  sample in the range of 4000 to 400  $\text{cm}^{-1}$  (see the black line) shows an absorption peak at 600–500  $\text{cm}^{-1}$  for Ti–O–Ti bond vibrations. A broad peak in the 3450–3350  $\text{cm}^{-1}$  range was assigned to the water adsorbed on the surface of  $\text{TiO}_2\text{NTs}$  (*i.e.*, moisture). The existing AC also showed absorption peaks for the several functional groups in its FT-IR spectrum (see the red line). These were mainly assigned to the stretching frequency of hydroxyl groups (at nearly 3400  $\text{cm}^{-1}$ ), alkyls (in the range of 2900–2800  $\text{cm}^{-1}$ ), carbonyls (at 1710  $\text{cm}^{-1}$ ), amides (at near 1650  $\text{cm}^{-1}$ ), and some other groups such as  $-\text{C}-\text{O}$  and  $\text{C}=\text{C}$  in the range of 1400–1000  $\text{cm}^{-1}$ . According to previous studies, these existing functional groups in the AC can be accounted for by its carbon (cellulosic) surface. Notably, the cellulosic surface could act as a host to accommodate the hydroxylated  $\text{TiO}_2\text{NTs}$ ; thus, the  $\text{TiO}_2\text{NTs-AC}$  nanocomposites were formed due to strong interaction between the AC and  $\text{TiO}_2\text{NTs}$ . The interaction between the AC and  $\text{TiO}_2\text{NTs}$  can be observed in the FT-IR spectra of the prepared NCs. The FT-IR spectra of NCs have shown all the corresponding peaks of unmodified AC and bare  $\text{TiO}_2\text{NTs}$ , along with slight shifting in their peak positions. Peak intensities were also found to be reduced in the nanocomposites. The shift in the peak positions and decrease in the intensity of IR absorption peaks are due to the interaction between

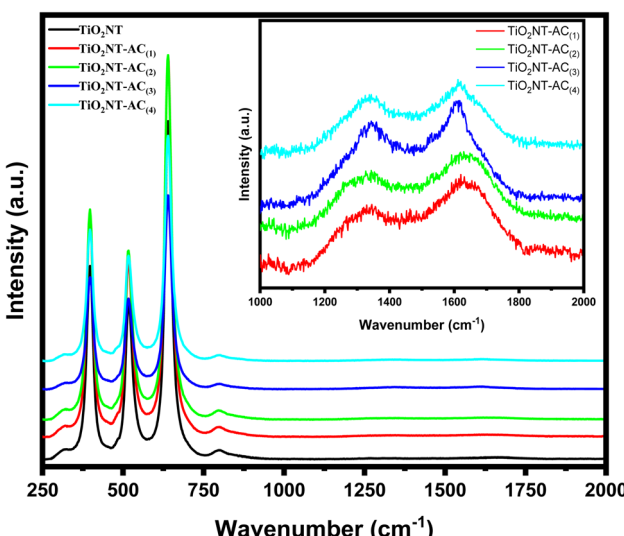


Fig. 2 Raman spectra of the prepared nanocomposites.



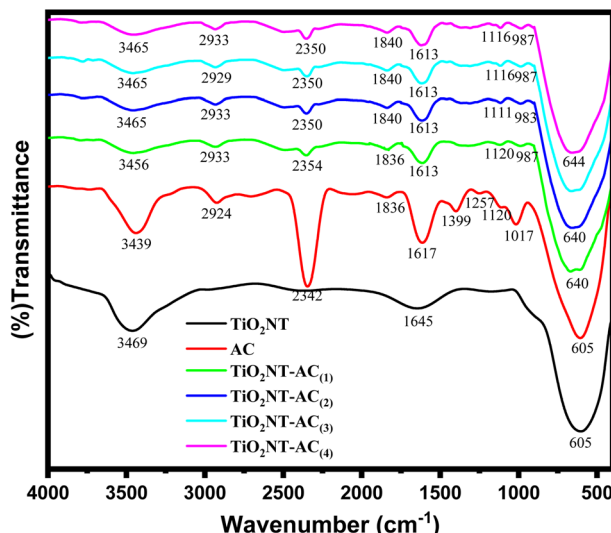


Fig. 3 FTIR spectra of the prepared nanocomposites.

the AC and  $\text{TiO}_2$ NTs *via*  $-\text{OH}$  functional groups. These observations suggest that the preparation of  $\text{TiO}_2$ NTs-AC nanocomposites is successful. The strength of the interaction of  $\text{TiO}_2$ NTs with AC increases with an increase in wt% of AC, which can also be confirmed by the lowering of peak intensities in their respective FT-IR spectra (20–40 wt% of AC). These results are in good agreement with previously reported research.<sup>34,35</sup>

#### 3.4. DR UV-vis spectroscopy

The solid-state diffuse reflectance UV-visible (DR UV-vis) spectra of the samples are shown in Fig. 4a. The spectrum of the bare  $\text{TiO}_2$ NT sample showed a characteristic absorbance at around 320–420 nm corresponding to the absorption edge at around 380 nm. On the other hand the  $\text{TiO}_2$ NTs-AC nanocomposite spectra showed two absorbance peaks centered at around 230 nm and 390 nm. This could be due to the effect of the presence of activated carbon species, which would absorb both UV and visible light. The  $\text{TiO}_2$ NTs-AC composites showed extended light absorption compared with the bare  $\text{TiO}_2$ NT sample. The absorption edges of  $\text{TiO}_2$ NTs-AC<sub>(1)</sub>,  $\text{TiO}_2$ NTs-AC<sub>(2)</sub>,  $\text{TiO}_2$ NTs-AC<sub>(3)</sub> and  $\text{TiO}_2$ NTs-AC<sub>(4)</sub> are found to be 428, 426, 422, and 415 nm respectively. The extended absorption for the synthesized composite samples is due to strong chemical interaction between the AC and  $\text{TiO}_2$ NTs. The bandgap energy of semiconducting materials plays an important role in photocatalytic applications. Narrow energy bandgap materials may be involved in light absorption's electronic excitation (valence bands to conduction bands). These excitations lead to hole formation and free electrons that reach the catalytic surface and are responsible for the photocatalytic properties. The bandgap energy can be tuned by altering the orientation of materials. In this study, the energy bandgap was measured for bare  $\text{TiO}_2$ NTs and  $\text{TiO}_2$ NTs-AC (10–40 wt%) samples using the data obtained from DR UV-vis analysis. The Tauc plots for the synthesized samples are shown in Fig. 4b–f. It was found that the energy bandgap of  $\text{TiO}_2$ NTs decreased slightly with an increase in

AC wt%, although the difference was found to be small. This is possibly due to the fact that there is no change in the crystal structure irrespective of deposition of AC on the surface of  $\text{TiO}_2$ NTs. The lowest bandgap (with a slight difference) was found for the highest content of AC in  $\text{TiO}_2$ NTs ( $\text{TiO}_2$ NTs-AC (wt% 40)) (Table 1).

#### 3.5. Photoluminescence (PL) spectroscopy

To clarify the migration and separation effectiveness of photo-generated charge carriers at the  $\text{TiO}_2$ NTs-AC nanocomposite interface, photoluminescence (PL) spectra were obtained. The semiconductors' electron–hole ( $e^- - h^+$ ) recombination is what causes the PL emission.<sup>36</sup> As a result, it is believed that the  $e^- - h^+$  recombination rate is directly proportional to the PL intensity. A lower PL intensity indicates a lower  $e^- - h^+$  recombination rate, indicating the examined photocatalyst's usefulness for photocatalytic processes.<sup>36</sup> Fig. 5 displays the PL spectra for the  $\text{TiO}_2$ NTs,  $\text{TiO}_2$ NTs-AC (wt% = 10), and  $\text{TiO}_2$ NTs-AC (wt% = 40) samples. In the visible range, the samples showed PL emission. The  $\text{TiO}_2$ NT sample exhibits a higher PL intensity than the  $\text{TiO}_2$ NTs-AC sample, as shown in Fig. 5. With an increase in the contents of AC (10 to 40% wt%), this intensity falls even further. Thus, it can be concluded that the  $e^- - h^+$  recombination rate lowers noticeably as the AC content increases, most likely because of the synergistic interaction between the AC and  $\text{TiO}_2$ NTs. This finding suggests that  $\text{TiO}_2$ NTs-AC could exhibit better photocatalytic performance than pure  $\text{TiO}_2$ NTs in the future. Additionally, the PL spectra offer compelling proof of the interaction between  $\text{TiO}_2$ NTs and AC.<sup>34</sup>

#### 3.6. HRTEM analysis

The HRTEM image (Fig. 6a) analysis revealed the development of bare anatase  $\text{TiO}_2$ NTs of various sizes (Table 1). The nanotubes have outer diameter around 5 and 7 nm and are 100–150 nm in length. The walls of the bare  $\text{TiO}_2$ NTs consist of 2 or 3 layers with an interlayer distance of 0.6 nm. The HRTEM image (Fig. 6c) of  $\text{TiO}_2$ NTs-AC suggested the presence of carbon on the surface of  $\text{TiO}_2$ NTs. The size of  $\text{TiO}_2$ NTs in  $\text{TiO}_2$ NTs-AC was smaller than that of bare  $\text{TiO}_2$ NTs, and breaking of the tubes into smaller ones could be observed. The lowering in the size of nanotubes could be due to the sonication treatment. The size of the tubes measured using TEM analysis is in agreement with the crystallite size calculated from the XRD analysis.

#### 3.7. XPS analysis

XPS is one of the most advanced techniques to determine the elements constituting the sample surface, its composition, and its chemical bonding state by analysing the energy of photo-electrons released upon X-ray interactions with the analysed sample. The existing sample was also subjected to the XPS analysis. The binding energy peak profile (high-resolution XPS spectrum) of the prepared sample is shown in Fig. 7. Single region binding energy profiles (such as C 1s, Ti 2p, and O 1s) for the  $\text{TiO}_2$ NTs-AC nanocomposite sample are shown in Fig. 7e–g. The critical energy profile of Ti ions is shown in Fig. 7e. Fig. 7e displays the two dominant peaks at 457.2 eV and 462.9 eV



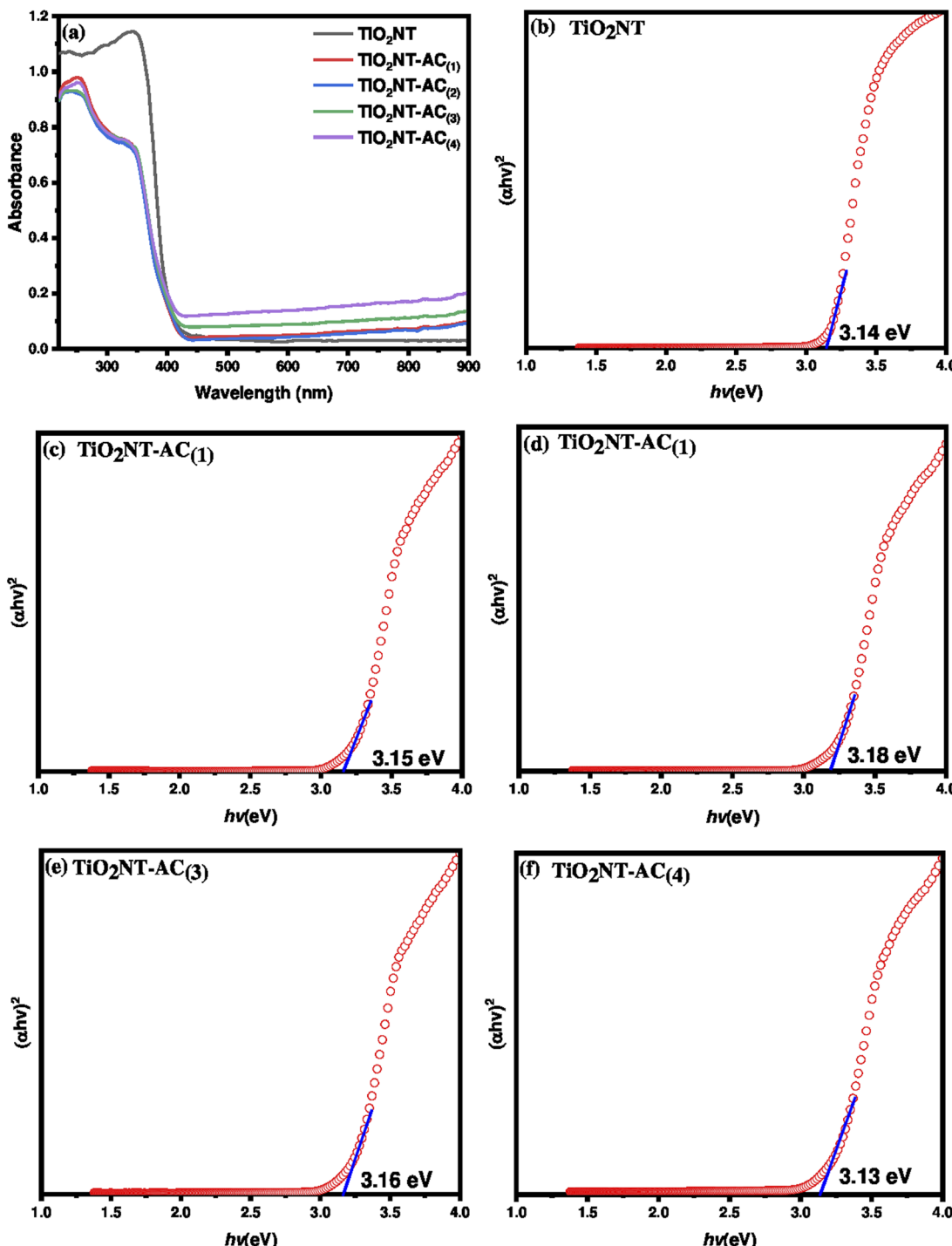


Fig. 4 (a) UV-visible diffuse reflectance spectra of pure  $\text{TiO}_2\text{NT}$  and  $\text{TiO}_2\text{NT-AC}$  nanocomposites and (b-f) results of the Tauc plot method for band gap calculation: (b) pure  $\text{TiO}_2\text{NT}$ , (c)  $\text{TiO}_2\text{NT-AC}_{(1)}$ , (d)  $\text{TiO}_2\text{NT-AC}_{(2)}$ , (e)  $\text{TiO}_2\text{NT-AC}_{(3)}$ , and (f)  $\text{TiO}_2\text{NT-AC}_{(4)}$ .

belonging to the Ti 2p doublets ( $\text{Ti } 2p_{3/2}$  and  $\text{Ti } 2p_{1/2}$ ). These doublets accounted for Ti ions' +4-oxidation state.<sup>5</sup> Notably, the  $\text{Ti } 2p_{3/2}$  binding energy peak of bare  $\text{TiO}_2\text{NTs}$  was assigned at 458.0 and 463.7 eV (Fig. 7c). Therefore, the shifting in the  $\text{Ti } 2p_{3/2}$  peak was observed in the XPS spectrum of prepared  $\text{TiO}_2\text{NTs-AC}$ .

Fig. 7f displays the binding peak at 530.5 eV for the O 1s region (lattice oxygen) related to the  $\text{TiO}_2\text{NTs}$  in the nanocomposites. It is found that the O 1s region binding energy

peaks of AC (533.5 eV in Fig. 7b) and bare  $\text{TiO}_2\text{NTs}$  (528.0 eV in Fig. 9d) were assigned in slightly different ranges (Fig. 7d), suggesting the shifting in the O 1s peak in the XPS spectrum of prepared  $\text{TiO}_2\text{NTs-AC}$ .<sup>34</sup> Fig. 7g displays the C1 region profile related to the AC in the nanocomposites. A binding energy peak at 284.0 eV is attributed to the carbon surface.<sup>34</sup> It should be noted that the C1 region profile related to the NC (Fig. 7g) displayed a slight difference from the C1 region profile related to



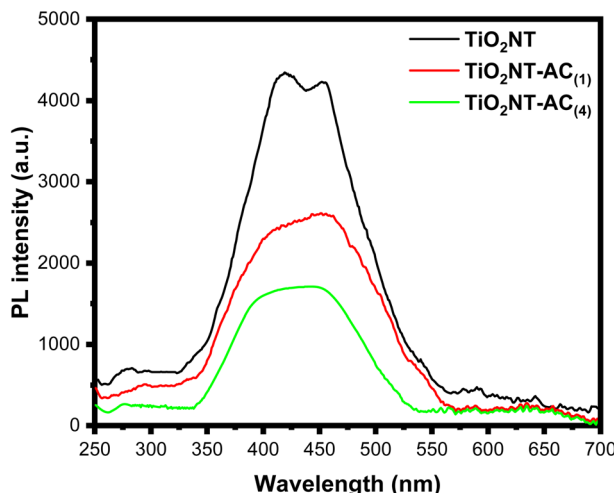


Fig. 5 Photoluminescence spectra of pure  $\text{TiO}_2\text{NT}$ ,  $\text{TiO}_2\text{NT-AC}_{(1)}$ , and  $\text{TiO}_2\text{NT-AC}_{(4)}$ .

the AC (Fig. 7a). These analyses, along with the shifting in the peaks, suggested the preparation of  $\text{TiO}_2\text{NTs-AC}$  *via* interaction between the AC and  $\text{TiO}_2\text{NTs}$ .

### 3.8. Nitrogen gas physisorption studies

The textural properties of the prepared  $\text{TiO}_2\text{NTs-AC}$  were investigated using  $\text{N}_2$  physisorption analysis (Fig. 8). The  $\text{N}_2$  adsorption–desorption isotherms for  $\text{TiO}_2\text{NTs-AC}$  adopt a type-III isotherm with an apparent  $\text{H}_3$  hysteresis loop as per IUPAC classification.<sup>34</sup> The type-III adsorption–desorption isotherm reflects the adsorbate's interaction with the adsorbent's surface.

The observed  $\text{H}_3$  hysteresis reflects  $\text{N}_2$  adsorption due to the capillary condensation, possibly due to the uneven distribution of aggregates in the sample with complex pore channels. The synthesized samples' pore size distribution (PSD) patterns were obtained using the NLDFT method. The results indicated the appearance of PSD peaks corresponding to macropores in  $\text{TiO}_2\text{NTs-AC}$ , probably due to the aggregation between particles forming large-size voids. The analysis reflected the specific surface area of  $\text{TiO}_2\text{NTs-AC}$ , which is listed in Table 1 with a pore volume and a half pore width.

### 3.9. Photocatalytic $\text{H}_2$ production over $\text{TiO}_2\text{NTs-AC}$ nanocomposites

Photoreforming of aqueous-methanol was assessed for the  $\text{H}_2$  production over the prepared material. This study was carried out with 100 mg of photocatalyst in pure water with methanol under uninterrupted artificial visible light irradiation for 6 h. This study shows the efficient photocatalytic properties of the prepared material. The  $\text{H}_2$  production has been observed under different conditions such as solution (water + catalyst) pH, catalyst dosage, reaction temperature and time, and the sacrificial agent's concentration such as methanol. The photocatalytic efficiency of the composite is compared with that of bare  $\text{TiO}_2\text{NTs}$  on all parameters. As can be seen, these results are shown in Fig. 9a–f. All the figures showed that the composite nanotubes showed a better hydrogen production rate under all conditions than the bare nanotubes.

Fig. 9a clearly shows that hydrogen production increases with the increase of time. In the first 2 hours, the hydrogen production concentration was  $\sim 1000.0$  and  $\sim 2300.0 \mu\text{mol}^{-1}$ , over the pure NTs and composite NTs, which increased to 4600

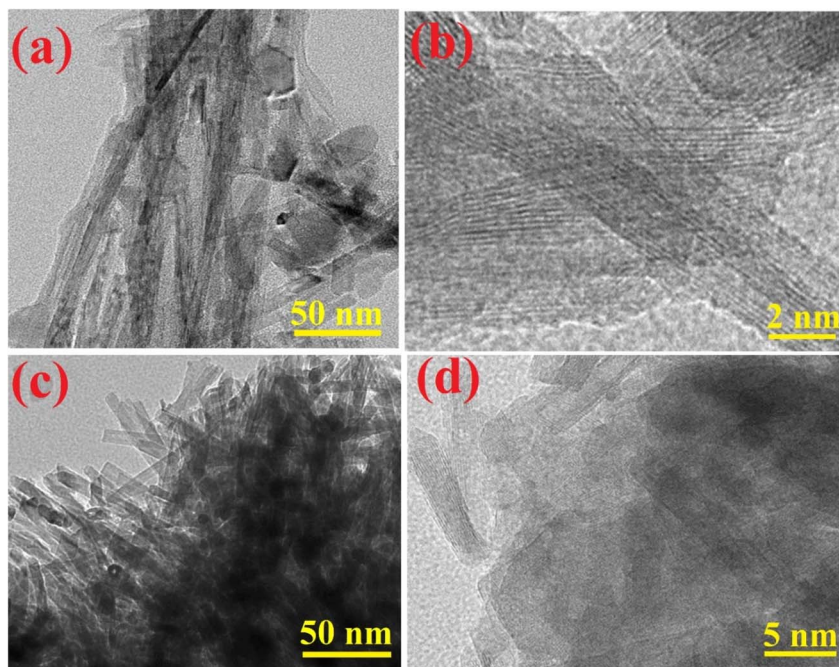


Fig. 6 TEM and HRTEM images of (a and b) pure  $\text{TiO}_2\text{NT}$  and (c and d)  $\text{TiO}_2\text{NT-AC}$  nanocomposites.



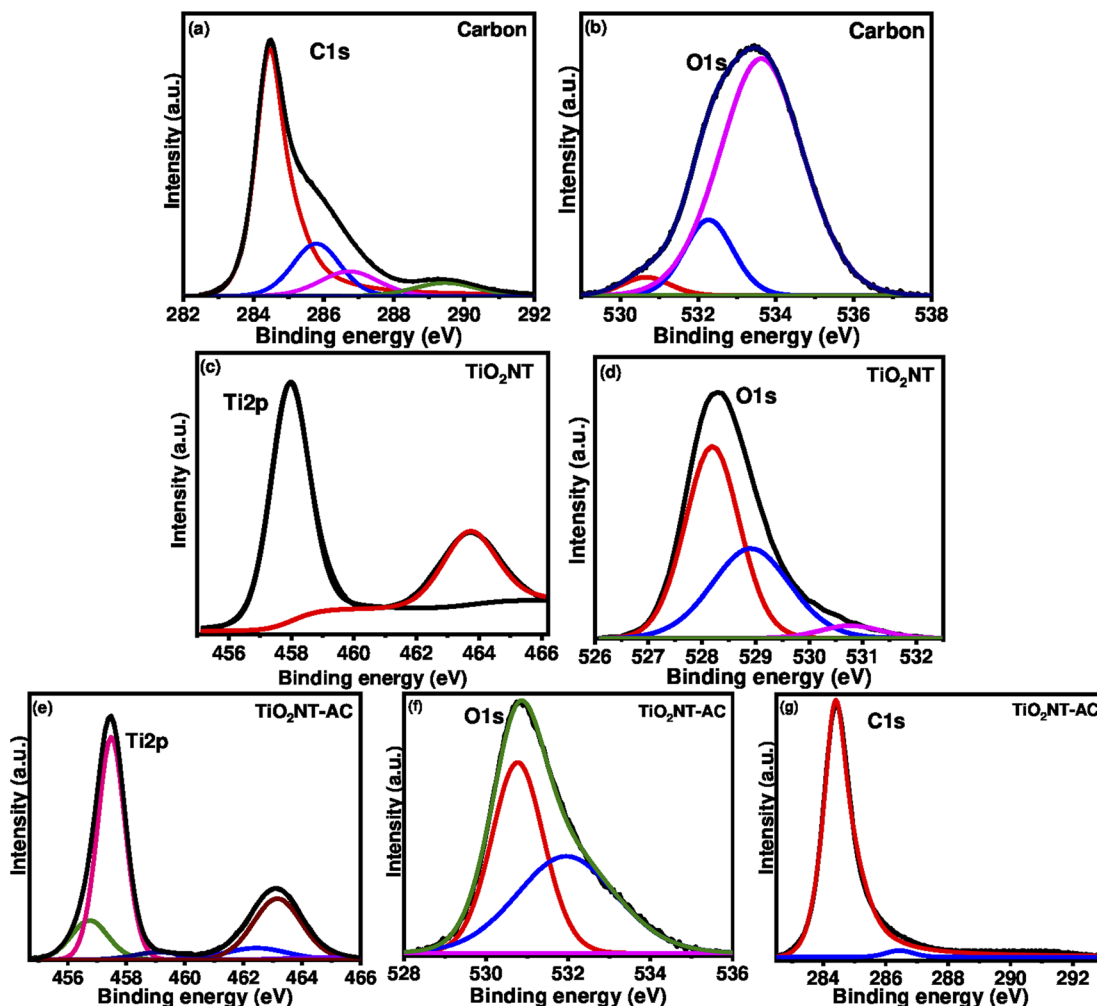


Fig. 7 Deconvoluted XPS spectra of AC, pure  $\text{TiO}_2\text{NT}$ , and  $\text{TiO}_2\text{NT-AC}$ .

and  $8500 \mu\text{mol}^{-1}$  after 6 hours, respectively. On doubling the reaction time, *i.e.*, after 12 hours, this production reached  $12\,000 \mu\text{mol}^{-1}$  and  $18\,000 \mu\text{mol}^{-1}$ . It can be seen from the figure that the composite nanotubes showed much better photocatalytic properties as compared to bare  $\text{TiO}_2\text{NTs}$ . Fig. 9b clearly shows that hydrogen production increases with an increase in the concentration of sacrificial agent methanol. At vol. 5% methanol, the hydrogen production concentration was  $\sim 3100$  and  $\sim 4900 \mu\text{mol}^{-1}$ , over the bare nanotubes and composite nanotubes, which increased to  $\sim 11\,900$  and  $18\,000 \mu\text{mol}^{-1}$  using 20 vol% methanol, respectively. After this, the equilibrium was attained for both materials and no efficient change was observed with a further increase in the methanol concentration. This result might be due to the surface blocking upon methanol loading, which declines the visible light absorption. Fig. 9c shows the pH effect result, which revealed that the  $\text{H}_2$  production rate was higher at basic pH than at acidic pH. However, the best thing is that both catalysts showed the best photocatalytic activity at neutral pH (the normal pH of water). As the acidic pH was attained (towards the lower pH  $< 7$ ), the hydrogen production rate decreased, and at pH = 3, the  $\text{H}_2$

production remained at only  $3460 \mu\text{mol}^{-1}$  and  $8900 \mu\text{mol}^{-1}$ , over the pure and composite nanotubes, respectively. These rates increased with an increase in the pH and, at pH 7, reached  $11\,940$  and  $17\,780 \mu\text{mol}^{-1}$ , which was much higher than that of acidic pH. On further increasing pH (towards the higher pH  $> 7$ ), the production rates decreased again, although it was almost negligible compared to acidic pH. At pH = 11,  $10\,420 \mu\text{mol}^{-1}$  and  $15\,950 \mu\text{mol}^{-1} \text{ H}_2$  were produced over the pure and composite nanotubes, respectively.

The hydrogen production rate was found to be higher with increased amounts of catalysts (Fig. 9d). Over 50 mg of bare and composite nanotubes,  $6400 \mu\text{mol}^{-1}$  and  $10\,625 \mu\text{mol}^{-1}$  hydrogen gas were produced *via* aqueous-methanol photoreforming, which was increased to  $14\,110$  and  $21\,230 \mu\text{mol}^{-1}$  at 200 mg of catalysts, respectively. However, it can also be seen that the  $\text{H}_2$  production rate increases rapidly in the beginning, but as the dose increases, the production rate slows down. Therefore, a slight increase in the  $\text{H}_2$  gas production ( $18\,000$  to  $21\,200 \mu\text{mol}^{-1}$ ) was observed after increasing the dose from 100 mg to 200 mg. The main reason for the rate slowing down with increasing dose can be considered to be an increase in



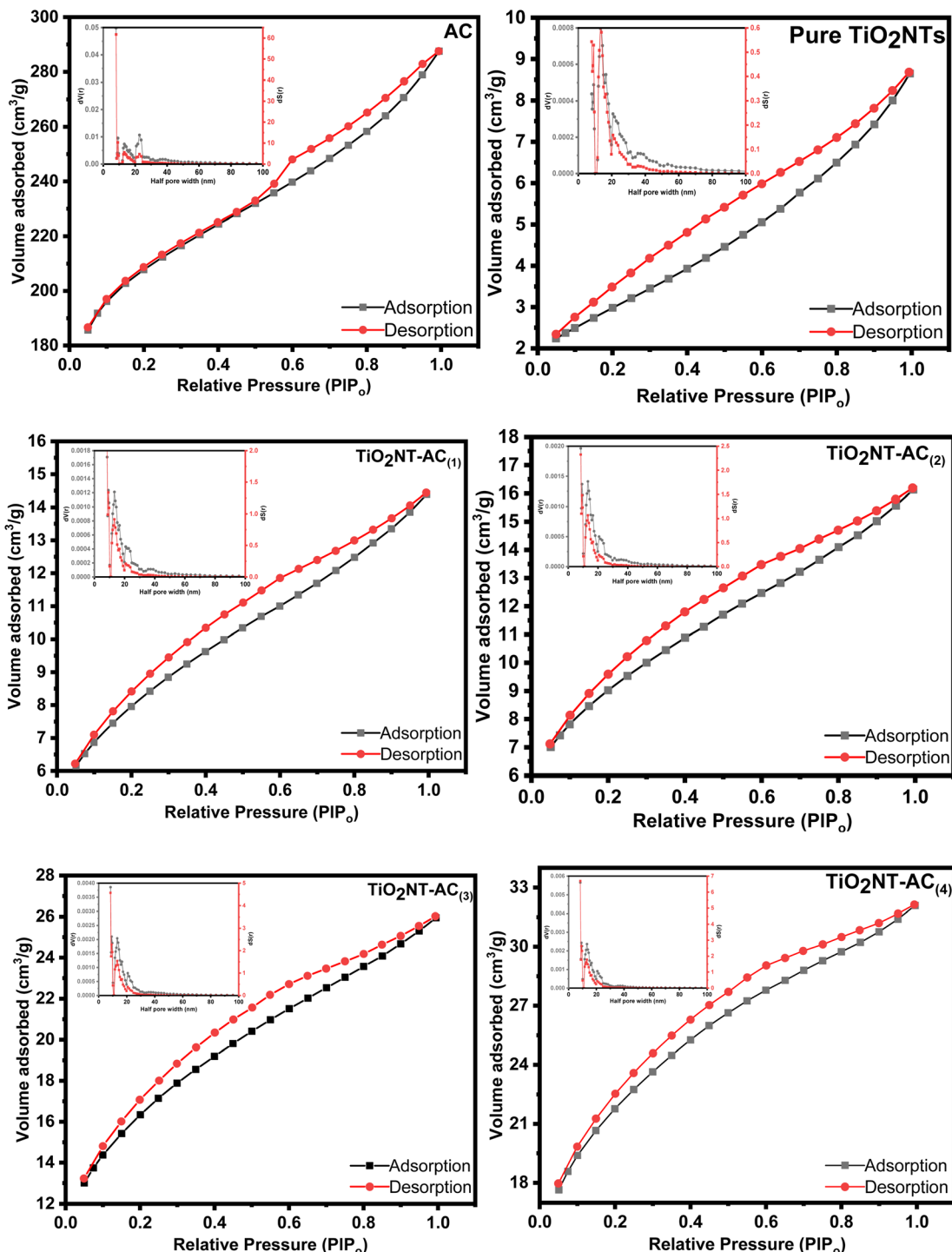


Fig. 8  $\text{N}_2$  adsorption–desorption isotherms and pore size distribution patterns (inset) of the synthesized samples.

light scattering rather than light absorption with increasing dose. Hence, possibly the visible light could not reach the active sites.

The temperature effect (25–55 °C) was also observed in the present study. The hydrogen production rate was found to be higher at the increased temperature (Fig. 9d). Approximately 12 000  $\mu\text{mol}^{-1}$  and 18 000  $\mu\text{mol}^{-1}$  hydrogen gas were produced

over pure and composite NTs at 25 °C, which reached up to 13 240 and 22 450  $\mu\text{mol}^{-1}$  at 45 °C, respectively. At a higher temperature (45 °C), only a slight change in the  $\text{H}_2$  production was observed for both catalysts. The actual efficiency of any material depends on its reusability. Therefore, reusability also reflects the sustainability of the material. Considering this as the basis, the reusability of composite NTs was also investigated

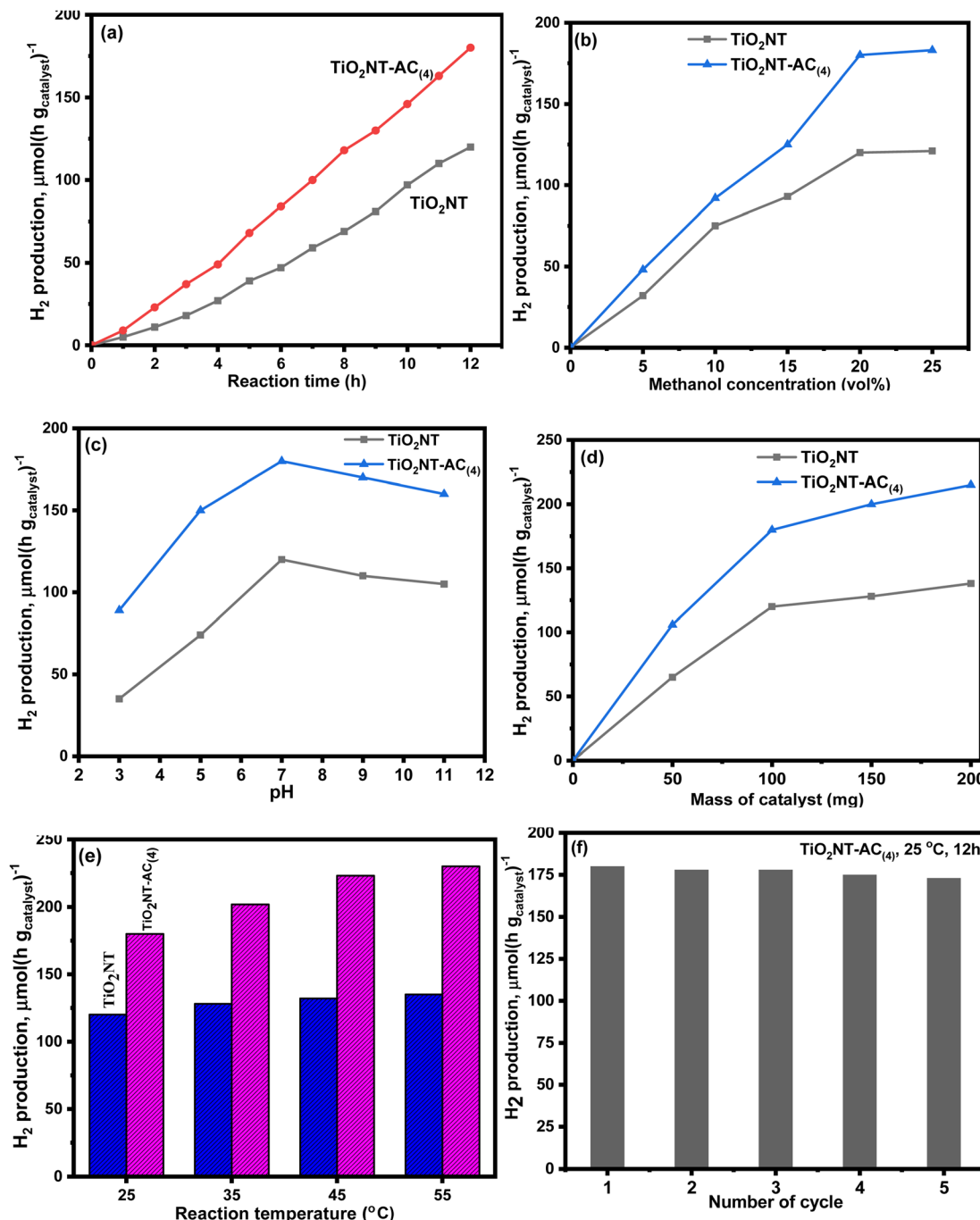


Fig. 9 Photocatalytic hydrogen production over synthesized TiO<sub>2</sub>NTs and TiO<sub>2</sub>NTs-AC<sub>(4)</sub> catalysts, (a) effect of reaction time, (b) effect of concentration of methanol, (c) effect of solution pH, (d) effect of mass of catalysts, (e) effect of reaction temperature, and (f) recyclability of the TiO<sub>2</sub>NTs-AC<sub>(4)</sub> catalyst.

in this study. This investigation was carried out for 5 consecutive cycles (Fig. 5f). Before reusing the composite nanotubes, the material was recovered by centrifugation after each cycle; then, it was washed with deionized water and dried by passing N<sub>2</sub> gas. After five cycles, the existing material showed only a slight decline in efficiency, which can be seen in Fig. 5f, so the existing material is useful for many processes. To investigate the structural stability of the catalyst, the XRD pattern of the spent

TiO<sub>2</sub>NTs-AC<sub>(4)</sub> catalyst was compared with that of the fresh catalyst. As shown in Fig. 10, the crystal structure of the catalyst was not altered after the reaction; however a slight change in the crystallinity of the sample was observed.

### 3.10. Plausible reaction mechanism for H<sub>2</sub> production

The whole mechanism of H<sub>2</sub> production can be understood using Scheme 2. When simulated sun light strikes the TiO<sub>2</sub>NTs-



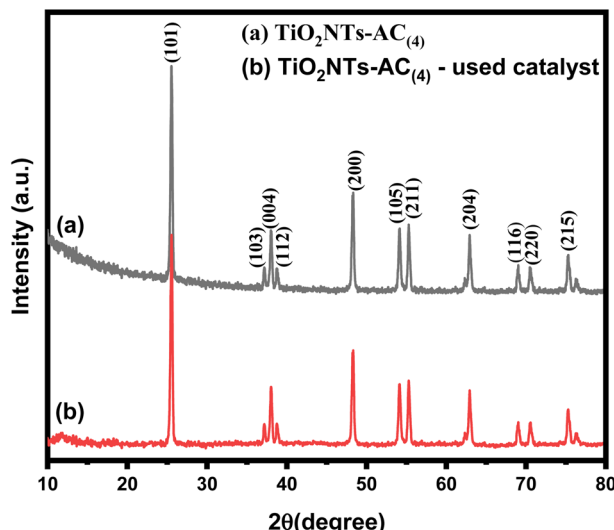
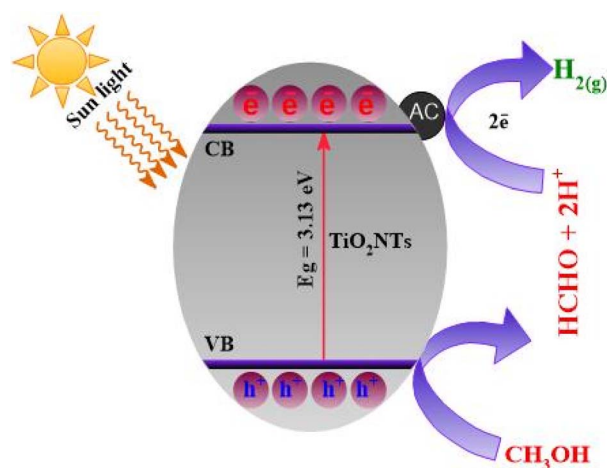
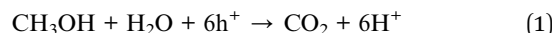


Fig. 10 Comparison of XRD patterns of fresh and spent  $\text{TiO}_2\text{NTs-AC}_{(4)}$  catalysts.



Scheme 2 Plausible reaction mechanism for  $\text{H}_2$  production over the  $\text{TiO}_2\text{NTs-AC}$  nanocomposite.

AC composite, holes ( $\text{h}^+$ ) and electrons ( $\text{e}^-$ ) are produced. The AC traps these photogenerated  $\text{e}^-$  from the CB of  $\text{TiO}_2\text{NTs}$ . This results in the distribution of electric charges across the semiconductor interface, which can prevent the recombination of charge carriers. The produced  $\text{e}^-$  and  $\text{h}^+$  on the surface of  $\text{TiO}_2\text{NTs-AC}$  react with the water and methanol adsorbed on the surface of  $\text{TiO}_2\text{NTs-AC}$  and produce the  $\text{H}_2$  gas, as shown in Scheme 2. It should be noted that the sacrificial agents may also serve as proton sources.<sup>5</sup> Therefore, using methanol can be considered for coupling an organic substance's oxidation and proton reduction. To investigate the pathway of photocatalytic reforming of aqueous methanol over the synthesized catalysts, the gaseous products were periodically analyzed using an online gas chromatograph equipped with a TCD and FID. The photocatalytic reformation of aqueous methanol solution mainly produced  $\text{H}_2$  in the gas phase and minor quantities of  $\text{CO}$ ,  $\text{CO}_2$  and  $\text{CH}_4$ . At the end of the photocatalytic test, the liquid phase was analyzed using a gas chromatograph equipped with both the FID and MSD. It is observed that methanol undergoes oxidation up to  $\text{CO}_2$  through the formation of formaldehyde and formic acid as intermediate species. As previously reported  $\text{CH}_3\text{OH}$  acts as a sacrificial agent and is oxidized by consumption of the photogenerated holes ( $\text{h}^+$ ) in the photocatalyst.<sup>7</sup> The photogenerated electrons ( $\text{e}^-$ ) are then used in the reduction of  $\text{H}^+$  to  $\text{H}_2$ . The presence of activated carbon with  $\text{TiO}_2$  decreased the recombination rate of the  $\text{e}^-$ - $\text{h}^+$  pairs, enhancing the photocatalytic activity of the catalyst.



A comparison of the photocatalytic activity of the  $\text{TiO}_2\text{NTs-AC}_{(4)}$  catalyst with that of other catalysts reported in the literature is presented in Table 2. The porous  $\text{TiO}_2\text{NTs-AC}_{(4)}$  nanocomposite offered high photocatalytic  $\text{H}_2$  rates compared to other  $\text{TiO}_2$  containing catalysts such as  $\text{TiO}_2$  anatase and  $\text{TiO}_2$ -AC catalysts. However, the  $\text{H}_2$  production rates are higher in the case of few other reported catalysts such as Pt-Cu/ $\text{TiO}_2$  catalysts compared to the  $\text{TiO}_2\text{NTs-AC}_{(4)}$  catalyst. It is essential to note

Table 2 Comparison of different photocatalysts reported for  $\text{H}_2$  production

S. no.	Photocatalyst	Sacrificial agent	Light source	$\text{H}_2$ production rate	Ref.
1	$\text{TiO}_2/\text{CuO}$	Methanol	Xe lamp	$8.23 \text{ mmol h}^{-1} \text{ g}^{-1}$	37
2	$\text{AC-TiO}_2$	Glycerol	Solar light	$20\,383 \mu\text{mol g}^{-1} \text{ h}^{-1}$	38
3	$\text{TiO}_2/\text{ACS}$	Glycerine	Solar light	$203 \mu\text{mol g}^{-1} \text{ h}^{-1}$	39
4	$\text{PtCu-TiO}_2$	Methanol	LED irradiation	$2383.9 \mu\text{mol h}^{-1}$	40
5	$\text{Pd-TiO}_2$	Ethanol	Near-UV light	$113 \text{ cm}^3 \text{ STP}$	16
6	$\text{Pd-TiO}_2$	Ethanol	Visible light	$29 \text{ cm}^3 \text{ STP}$	16
7	$\text{Ni/GO-TiO}_2$	Methanol	UV light	$2171 \mu\text{mol h}^{-1} \text{ g}^{-1}$	41
8	$\text{CuO/TiO}_2\text{NT}$	Methanol	Mercury lamp	$64.2\text{--}71.6 \text{ mmol h}^{-1} \text{ g}^{-1}$	42
9	$\text{SnS}_2/\text{TiO}_2$	Methanol	Solar irradiation	$195.55 \mu\text{mol g}^{-1}$	21
10	$\text{Pt-TiO}_2$	Methanol	UV mercury lamp	$38.0 \text{ mmol g}^{-1} \text{ h}^{-1}$	43
11	$\text{TiO}_2\text{NTs-AC}$	Methanol	Solar light	$18\,000 \mu\text{mol}^{-1} \text{ g}^{-1} \text{ h}^{-1}$	Present work

that the presence of precious and transition metals and physicochemical characteristics of previously reported catalysts and reaction conditions are different from those of the present work. Moreover, the present research deals with deposition of activated carbon over  $\text{TiO}_2$  nanotubes *via* ultrasonication and utilized the synthesized materials for photocatalytic reformation of methanol to produce  $\text{H}_2$ .

## 4. Conclusions

In this study,  $\text{TiO}_2$  nanotubes are combined with activated carbon derived from biomass to obtain  $\text{TiO}_2\text{NTs-AC}$  nanocomposites. The synthesized materials showed high water-splitting efficiency, under sunlight which proved to be energy efficient for hydrogen production. The synthesized composites are porous in nature (pore volume =  $0.020\text{ cm}^3\text{ g}^{-1}$  and half pore width =  $8.4\text{ \AA}$ ) and nanosized (crystallite size =  $6.31\text{ nm}$ ) with a high surface area ( $291\text{ m}^2\text{ g}^{-1}$ ). Its band gap was measured to be  $3.15\text{ eV}$ . The prepared material produced approximately  $18\,000\text{ }\mu\text{mol}^{-1}$  of hydrogen gas using  $100\text{ mg}$  of catalyst at pH 7 and  $25\text{ }^\circ\text{C}$  under 12 hours of continuously simulated sun light irradiation. The material also showed a high reusability rate. Furthermore, the prepared nanocomposite was used for up to 5 cycles without a significant decrease, indicating its good efficiency and sustainability. Furthermore, photocatalytic activity can be influenced by the light absorption, redox nature, and mass transfer of the process, therefore, some more studies are needed to understand the influence of these factors and obtain efficient results. In addition, synthesis of activated carbon needs high energy utilization and release of air pollutants; hence, some more low cost and abundant alternatives can be searched, in the future.

## Author contributions

All authors contributed to the study conception and design. Material preparation, data collection and analysis were performed by Shaeel Ahmed Althabaiti Zaheer Khan, Maqsood Ahmad Malik, Salem Mohamed Bawaked, Soad Zahir Al-Sheheri, and Mohamed Mokhtar. The first draft of the manuscript was written by Sharf Ilahi Siddiqui, Maqsood Ahmad Malik, and Katabathini Narasimharao and all authors commented on previous versions of the manuscript. All authors read and approved the final manuscript.

## Conflicts of interest

There are no conflicts of interest to declare.

## Acknowledgements

The authors extend their appreciation to the Deputyship for Research & Innovation, Ministry of Education in Saudi Arabia for funding this research work through the project number IFPNC-001-130-2020 and Deanship of Scientific Research (DSR), King Abdulaziz University, Jeddah, Saudi Arabia.

## References

- 1 L. Schlapbach and A. Züttel, *Nature*, 2001, **414**, 353–358.
- 2 J. L. Rowsell and O. M. Yaghi, *Angew. Chem., Int. Ed.*, 2005, **44**, 4670–4679.
- 3 J. Yang, A. Sudik, C. Wolverton and D. J. Siegel, *Chem. Soc. Rev.*, 2010, **39**, 656–675.
- 4 S. P. Badwal, S. Giddey and C. Munnings, *Wiley Interdiscip. Rev.: Energy Environ.*, 2013, **2**, 473–487.
- 5 K. C. Christoforidis and P. Fornasiero, *ChemCatChem*, 2017, **9**, 1523–1544.
- 6 L. Fan, Z. Tu and S. H. Chan, *Energy Rep.*, 2021, **7**, 8421–8446.
- 7 J. Wen, J. Xie, X. Chen and X. Li, *Appl. Surf. Sci.*, 2017, **391**, 72–123.
- 8 T. Shen, H. Xie, B. Gavurová, M. Sangeetha, C. Karthikeyan, T. R. Praveenkumar, C. Xia and S. Manigandan, *Int. J. Hydrogen Energy*, 2023, **48**, 21029–21037.
- 9 L. Chen, H. Li, H. Wang and K. Liu, *J. Cleaner Prod.*, 2023, 137213.
- 10 X. Shui, D. Jiang, Y. Li, H. Zhang, J. Yang, X. Zhang and Q. Zhang, *Bioresour. Technol.*, 2023, **367**, 128221.
- 11 P. Vargas-Ferrer, E. Álvarez-Miranda, C. Tenreiro and F. Jalil-Vega, *J. Cleaner Prod.*, 2023, **409**, 137110.
- 12 G. Liu, H. Lu, Y. Xu, Q. Quan, H. Lv, X. Cui, J. Chen, L. Jiang and R. J. Behm, *Chem. Eng. J.*, 2023, **455**, 140875.
- 13 D. Aand, S. Sk, K. Kumar, U. Pal and A. K. Singh, *Int. J. Hydrogen Energy*, 2022, **47**, 7180–7188.
- 14 J. Talibawo, P. I. Kyesmen, M. C. Cyulinyana and M. Diale, *Nanomaterials*, 2022, **12**, 2961.
- 15 Q. Cao, S. Hao, Y. Wu, K. Pei, W. You and R. Che, *Chem. Eng. J.*, 2021, **424**, 130444.
- 16 B. Rusinque, S. Escobedo and H. de Lasa, *Catalysts*, 2021, **11**, 405.
- 17 G. L. Chiarello, M. V. Dozzi and E. Selli, *J. Energy Chem.*, 2017, **26**, 250–258.
- 18 J. Yu, L. Qi and M. Jaroniec, *J. Phys. Chem. C*, 2010, **114**, 13118–13125.
- 19 R. Saravanan, D. Manoj, J. Qin, M. Naushad, F. Gracia, A. F. Lee, M. M. Khan and M. Gracia-Pinilla, *Process Saf. Environ. Prot.*, 2018, **120**, 339–347.
- 20 D. Xu, Y. Hai, X. Zhang, S. Zhang and R. He, *Appl. Surf. Sci.*, 2017, **400**, 530–536.
- 21 S. Shanmugaratnam, B. Selvaratnam, A. Baride, R. Koodali, P. Ravirajan, D. Velauthapillai and Y. Shivatharsiny, *Catalysts*, 2021, **11**, 589.
- 22 H. Song, S. Luo, H. Huang, B. Deng and J. Ye, *ACS Energy Lett.*, 2022, **7**, 1043–1065.
- 23 A. H. Jawhari, N. Hasan, I. A. Radini, K. Narasimharao and M. A. Malik, *Nanomaterials*, 2022, **12**, 2985.
- 24 S. A. Althabaiti, M. A. Malik, M. Kumar Khanna, S. M. Bawaked, K. Narasimharao, S. Z. Al-Sheheri, B. Fatima and S. I. Siddiqui, *Nanomaterials*, 2022, **12**, 4472.
- 25 M. Ouzzine, A. J. Romero-Anaya, M. A. Lillo-Rodenas and A. Linares-Solano, *Carbon*, 2014, **67**, 104–118.
- 26 M. Asiltürk and S. Şener, *Chem. Eng. J.*, 2012, **180**, 354–363.



27 B. Mondol, A. Sarker, A. Shareque, S. C. Dey, M. T. Islam, A. K. Das, S. M. Shamsuddin, M. A. I. Molla and M. Sarker, *Photochem.*, 2021, **1**, 54–66.

28 K. Li, H. Ruan, P. Ning, C. Wang, X. Sun, X. Song and S. Han, *Res. Chem. Intermed.*, 2018, **44**, 1209–1233.

29 L. Cui, K. Hui, K. Hui, S. Lee, W. Zhou, Z. Wan and C.-N. H. Thuc, *Mater. Lett.*, 2012, **75**, 175–178.

30 A. H. Jawhari, N. Hasan, I. A. Radini, M. A. Malik and K. Narasimharao, *Fuel*, 2023, **344**, 127998.

31 X.-Y. Liu, M. Huang, H.-L. Ma, Z.-Q. Zhang, J.-M. Gao, Y.-L. Zhu, X.-J. Han and X.-Y. Guo, *Molecules*, 2010, **15**, 7188–7196.

32 Z. Dong, F. Xiao, A. Zhao, L. Liu, T. Sham and Y. Song, *RSC Adv.*, 2016, **6**, 76142–76150.

33 E. Ribeiro, G. Plantard, F. Teyssandier, F. Maury, N. Sadiki, D. Chaumont and V. Goetz, *J. Environ. Chem. Eng.*, 2020, **8**, 104115.

34 Y. G. Alghamdi, B. Krishnakumar, M. A. Malik and S. Alhayyani, *Polymers*, 2022, **14**, 880.

35 S. Muthusamy and J. Charles, *J. Mater. Sci.: Mater. Electron.*, 2021, **32**, 7349–7365.

36 Y. Feng, C. Liu, J. Chen, H. Che, L. Xiao, W. Gu and W. Shi, *RSC Adv.*, 2016, **6**, 38290–38299.

37 J. M. Kum, S. H. Yoo, G. Ali and S. O. Cho, *Int. J. Hydrogen Energy*, 2013, **38**, 13541–13546.

38 N. R. Reddy, U. Bharagav, M. M. Kumari, K. Cheralathan, P. Ojha, M. Shankar and S. W. Joo, *Ceram. Int.*, 2021, **47**, 10216–10225.

39 G. Murali, S. Gopalakrishnan, S. K. Lakhera, B. Neppolian, S. Ponnusamy, S. Harish and M. Navaneethan, *Diamond Relat. Mater.*, 2022, **128**, 109226.

40 H. Wang, H. Qi, X. Sun, S. Jia, X. Li, T. J. Miao, L. Xiong, S. Wang, X. Zhang and X. Liu, *Nat. Mater.*, 2023, 1–8.

41 O. Quiroz-Cardoso, V. Suárez, S. Oros-Ruiz, M. Quintana, S. Ramírez-Rave, M. Suárez-Quezada and R. Gómez, *Top. Catal.*, 2022, **65**, 1015–1027.

42 S. Xu, A. J. Du, J. Liu, J. Ng and D. D. Sun, *Int. J. Hydrogen Energy*, 2011, **36**, 6560–6568.

43 J. Velázquez, R. Fernández-González, L. Díaz, E. P. Melián, V. Rodríguez and P. Núñez, *J. Alloys Compd.*, 2017, **721**, 405–410.

